Supporting Information for:

Degradation of bifunctional α-MnO_2/NiO@Ni gas-diffusion electrodes for Zn-air batteries: space-resolved Ni chemical-state evolution mapped by Soft X-ray Spectral Ptychography

Alessandro Alleva[a,*], Francesco Guzzi[b], Massimo Frittelli[c], George Kourousias[b], Valentina Bonanni[b], Alessandra Gianoncelli[b], Ivonne Sgura[c], Milan Žižić[b] and Benedetto Bozzini[a]

[a]Department of Energy, Politecnico di Milano, via Lambruschini 4, Milano 20156, Italy
[b]Elettra - Sincrotrone Trieste S.C.p.A. S.S, 14, km 163.5 in Area Science Park, Trieste-Basovizza 34149, Italy
[c]Università del Salento, Dipartimento di Matematica e Fisica "E. De Giorgi", via per Arnesano, 73100 Lecce, Italy

S1. Phase-to-Magnitude Conversion via Kramers–Kronig Transform

The reconstruction of absorption spectra from phase contrast images obtained via ptychography was carried out using the computational procedure based on the Kramers–Kronig (KK) transform, as presented by Watts [1]. The algorithm employs a piecewise Laurent polynomial approximation of the absorption spectrum to evaluate the KK integral efficiently. In this work, the Python library KKcalc (developed by Watts) was adapted to process phase spectra acquired at the Ni L-edge. The procedure consisted of selecting a region of interest (ROI), averaging the extracted phase shift δ(E), and computing the corresponding synthetic absorption spectrum β(E).

S2. Cosine Similarity Classification

Pixel classification was performed by comparing each local spectrum to a reference spectrum using cosine similarity:

$$\text{cosine similarity}(x, y) = \frac{\sum_i x_i y_i}{\sqrt{\sum_i x_i^2}\sqrt{\sum_i y_i^2}}$$

This metric was chosen due to its emphasis on spectral shape over absolute peak positions, which may vary slightly due to local energy shifts. An heuristic threshold of 0.85 was set, allowing to reliably exclude outlier spectra without discarding physically meaningful spectra. The following Python function was used:

```
def compute_cosine_similarity_map(stack, reference_spectrum):
    y_dim, x_dim = stack.shape[1:]
    similarity_map = np.zeros((y_dim, x_dim))
    for y in range(y_dim):
        for x in range(x_dim):
            pixel_spectrum = stack[:, y, x].reshape(1, -1)
```

```
            similarity           =           cosine_similarity(pixel_spectrum,
reference_spectrum.reshape(1, -1))[0][0]
            similarity_map[y, x] = similarity
    return similarity_map
```

S3. Label-Based Pixel Classification

Combined classification maps were built by merging the magnitude and phase similarity masks into four categories: background, phase only, magnitude only, and both. The implementation used was:

```
def coloring(matrix):
    a = np.zeros(matrix[0].shape, dtype=int)
    for i in range(matrix[0].shape[0]):
        for j in range(matrix[0].shape[1]):
            if matrix[0, i, j] == 0 and matrix[1, i, j] == 0:
                a[i, j] = 1  # Background
            elif matrix[0, i, j] == 1 and matrix[1, i, j] == 0:
                a[i, j] = 2  # Phase Only
            elif matrix[0, i, j] == 0 and matrix[1, i, j] == 1:
                a[i, j] = 3  # Magnitude Only
            elif matrix[0, i, j] == 1 and matrix[1, i, j] == 1:
                a[i, j] = 4  # Both
    return a
```

S4. Reconstruction of Hybrid Stacks

For each pixel, the classification map determined whether the magnitude spectrum, the KK-transformed phase spectrum, or no data was assigned. The function below was used to reconstruct the absorption-equivalent stack:

```
def build_stack_from_label_mask(mask_label, mag, phase, energies, export_path,
element='Ni'):
    e_len, x_size, y_size = mag.shape
    out_stack = np.zeros((e_len, x_size, y_size), dtype=np.float32)

    mask_label = np.squeeze(mask_label)
    if mask_label.shape != (x_size, y_size):
        raise ValueError(f"Wrong mask dimension: {mask_label.shape}, expected
({x_size}, {y_size})")

    for i in range(x_size):
        for j in range(y_size):
            try:
                label = mask_label[i, j]
                print(f"→ label ({i},{j}) = {label} (type: {type(label)})")

                if label == 1:
```

```
                    out_stack[:, i, j] = 0

                elif label in (3, 4):
                    out_stack[:, i, j] = mag[:, i, j]

                elif label == 2:
                    phase_pixel = phase[:, i, j]
                    print(f"→ phase shape: {phase_pixel.shape}, type:
{type(phase_pixel)}")

                    if not np.all(np.isfinite(phase_pixel)):
                        print(f" Non valid data in pixel ({i},{j}) → skip")
                        continue

                    real_part = kk_real_from_arrays(energies, phase_pixel,
element=element)
                    out_stack[:, i, j] = real_part

            except Exception as e:
                print(f" Error in pixel ({i},{j}): {e}")
                out_stack[:, i, j] = 0
```

The whole hybrid map reconstruction workflow is summarized in Fig. S1

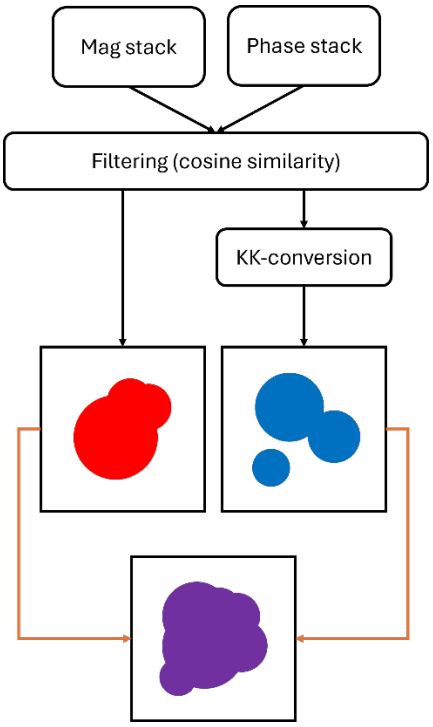


Fig. S1 – Schematic of the workflow for the reconstruction of hybrid maps. After filtering, the phase spectra are converted to absorption spectra using the KK relations. The resulting KK-derived

spectra are then compared with the filtered magnitude stack, and the two datasets are merged by assigning the KK-converted phase spectra to the pixels where no reliable magnitude spectra were available.

S5. Electrochemical Impedance Spectrometry Analysis

Electrochemical impedance spectrometry was employed to monitor the evolution of the electrochemical response of the gas diffusion electrodes during GDC ageing and to provide an electrochemical descriptor complementary to the GDC quantifiers (see Figure 7) and spectromicroscopy observations (Section 3.3) discussed in the main manuscript. The impedance spectra were analysed using the equivalent-circuit methodology described in the Materials and Methods section. The acquisition points adopted during the GCD ageing protocol are indicated in Fig. S2, while the complete correspondence between ageing steps and EIS measurements is reported in Table S1.

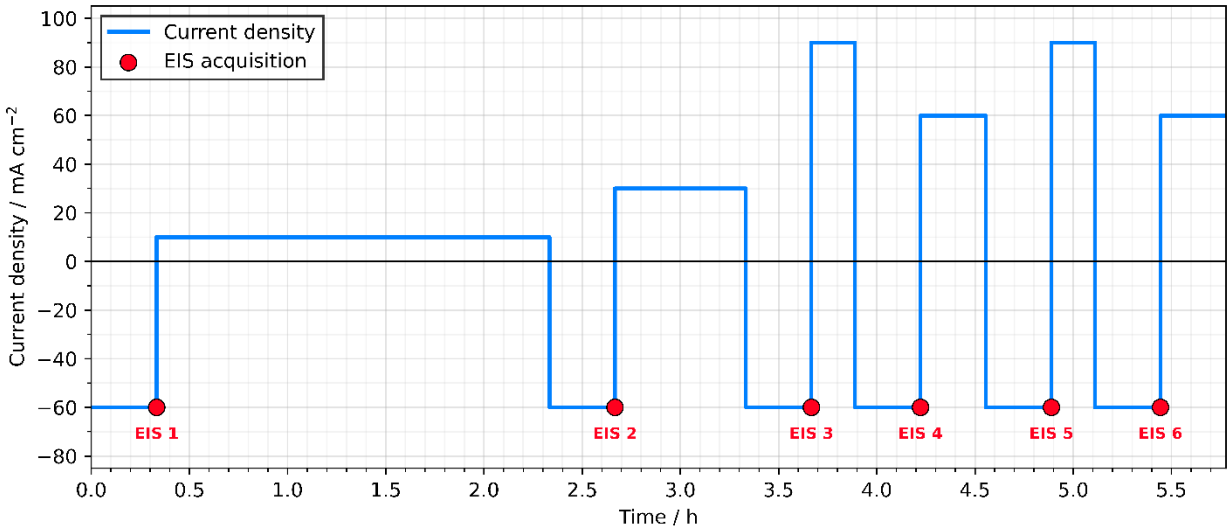


Fig. S2 – GCD ageing protocol used for the investigated GDEs. Blue line: applied current density profile. Red markers indicate the time points at which electrochemical impedance spectrometry measurements were acquired.

Step number	**EIS in RSP cycle**
1	EIS 1
2	EIS 2
3	EIS 3
4	EIS 4
5	EIS 5
6	EIS 6
7-12	Same sequence during cycle 2
13-18	Same sequence during cycle 3

Table S1 - Correspondence between the RSP step numbers and the EIS labels reported in the graphs

The spectra were analysed using an equivalent-circuit approach aimed at extracting comparable resistive descriptors throughout ageing, rather than at providing a unique physical deconvolution of all processes occurring within the porous gas-diffusion electrode. A single-time-constant circuit,

M1 = $R_s - (R_{ct} \parallel CPE)$,

was initially considered. However, most spectra were more accurately described by a two-time-constant model,

M2 = $R_s - (R_1 \parallel CPE_1) - (R_2 \parallel CPE_2)$,

which was therefore adopted as the main fitting framework. The series resistance R_s was taken as the overall ohmic contribution of the cell, including electrolyte, contacts and electronic/ionic continuity within the electrode assembly. The polarization resistance was defined as:

$R_{pol} = R_1 + R_2$

and was used as the primary quantitative descriptor of electrode evolution.
Frequencies above 5 kHz were excluded from the fitting window. In highly porous GDEs, the very high-frequency region is strongly affected by ohmic/contact contributions and distributed capacitive effects, which provide limited direct information on the electrocatalytic response and oxygen transport through the electrode architecture. Restricting the fitting window improved fit stability and parameter comparability while focusing the analysis on the frequency range most relevant to the electrochemical processes of interest. Although some spectra exhibited features potentially compatible with more than two relaxation processes, the introduction of additional circuit elements would have substantially increased the number of free parameters and the associated risk of overfitting. The M2 model was therefore retained as a consistent comparative framework for the entire dataset. Because the two relaxation processes were not equally distinguishable in all spectra, a diagnostic classification procedure was developed to evaluate the degree of process separation. Each spectrum was assigned a score based on five criteria:

I. improvement of the M2 fit relative to M1 by at least 30% in terms of relative RMSE;
II. separation between the characteristic frequencies of the two branches of at least 0.5 decades;
III. contribution of the smaller resistive branch equal to at least 10% of the total polarization resistance;
IV. maximum relative 95% confidence interval of the fitted resistances not exceeding 100%;

V. both characteristic frequencies located within the experimental frequency window.

Spectra scoring 4–5 points were classified as resolved, spectra scoring 2–3 points as borderline and spectra scoring 0–1 points as collapsed. The resulting classification map is reported in Fig. S3.

The resolved/borderline/collapsed classification was introduced primarily as a diagnostic indicator of parameter identifiability. Nevertheless, the loss of separability may also reflect a progressive convergence of the characteristic timescales associated with the dominant electrochemical processes occurring within the porous electrode. Representative examples of the three categories are shown in Fig. S4. In resolved spectra, the two relaxation processes are clearly distinguishable and the M2 model provides a physically meaningful separation of the resistive contributions. In borderline spectra, the two processes remain partially identifiable but increasing overlap results in larger uncertainties. In collapsed spectra, the electrochemical response approaches that of a single dominant relaxation process and the physical interpretation of the individual branches becomes unreliable.

Importantly, this classification was not used to modify the extraction of the quantitative ageing descriptors. The polarization resistance employed throughout the manuscript remained defined as $R_{pol} = R_1 + R_2$ for all spectra. The resolved/borderline/collapsed classification was used only to assess whether the individual contributions R_1 and R_2 could be discussed as separate physical processes.

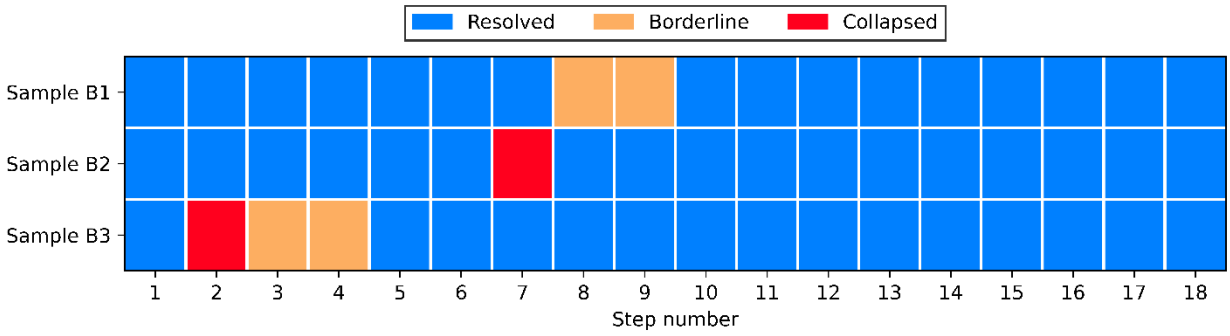


Fig. S3 - Diagnostic classification of impedance spectra according to the degree of separation between the two relaxation processes described by the M2 equivalent circuit. Blue: resolved spectra (score 4–5), where the two processes are clearly distinguishable. Orange: borderline spectra (score 2–3), where the processes are only partially separated. Red: collapsed spectra (score 0–1), where a reliable physical distinction between the two branches is no longer possible.

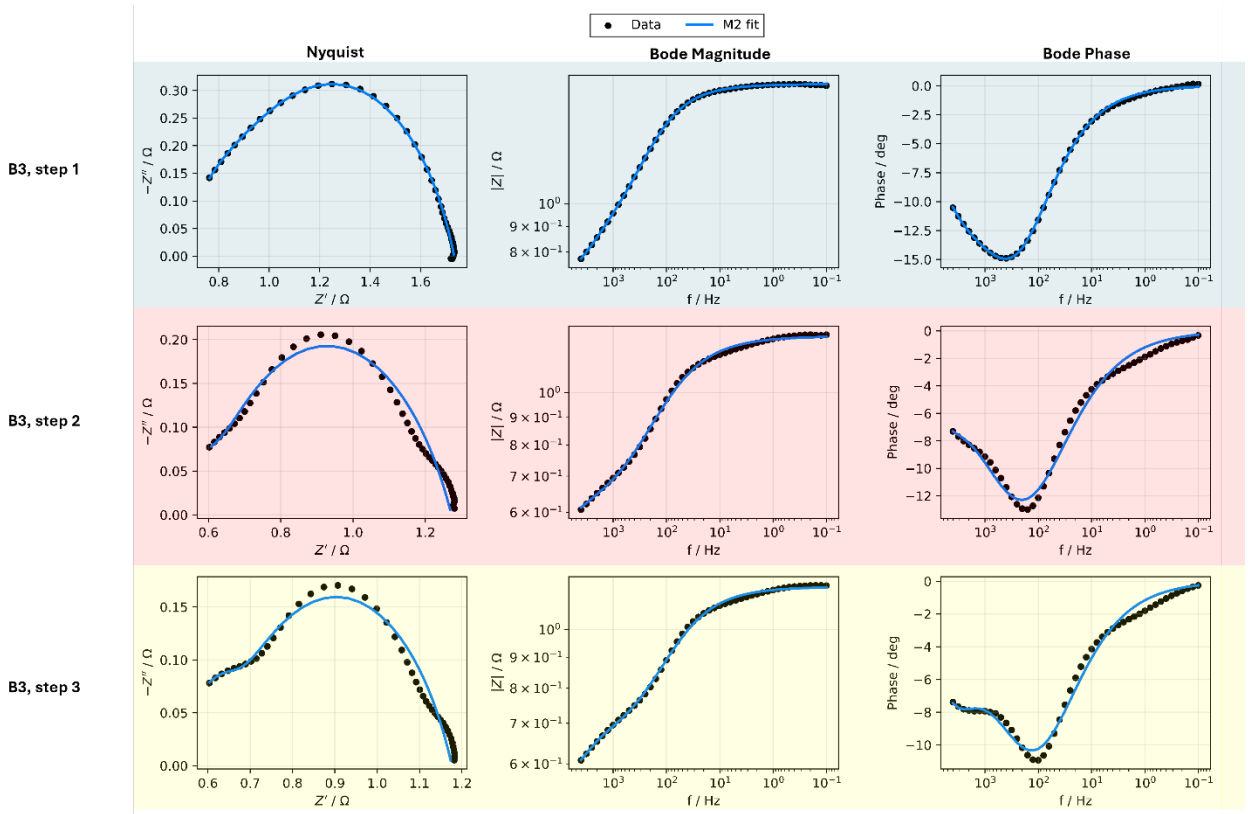


Fig. S4 - Representative examples of resolved (top row), collapsed (middle row) and borderline (bottom row) impedance spectra together with the corresponding M2 equivalent-circuit fits. For each case, Nyquist (left), Bode magnitude (centre) and Bode phase (right) representations are reported.

The evolution of R_s during ageing is shown in Fig. S5. For all electrodes, the series resistance remained within a relatively limited range compared to the changes observed for the polarization resistance, indicating that the dominant ageing effects occurred within the electrochemical response of the electrode rather than through major variations in electrolyte conductivity or contact resistance. The complete quantitative evolution of R_s and R_{pol} throughout ageing is summarized in Table S2. These data provide the detailed numerical values underlying the trends discussed in the main manuscript.

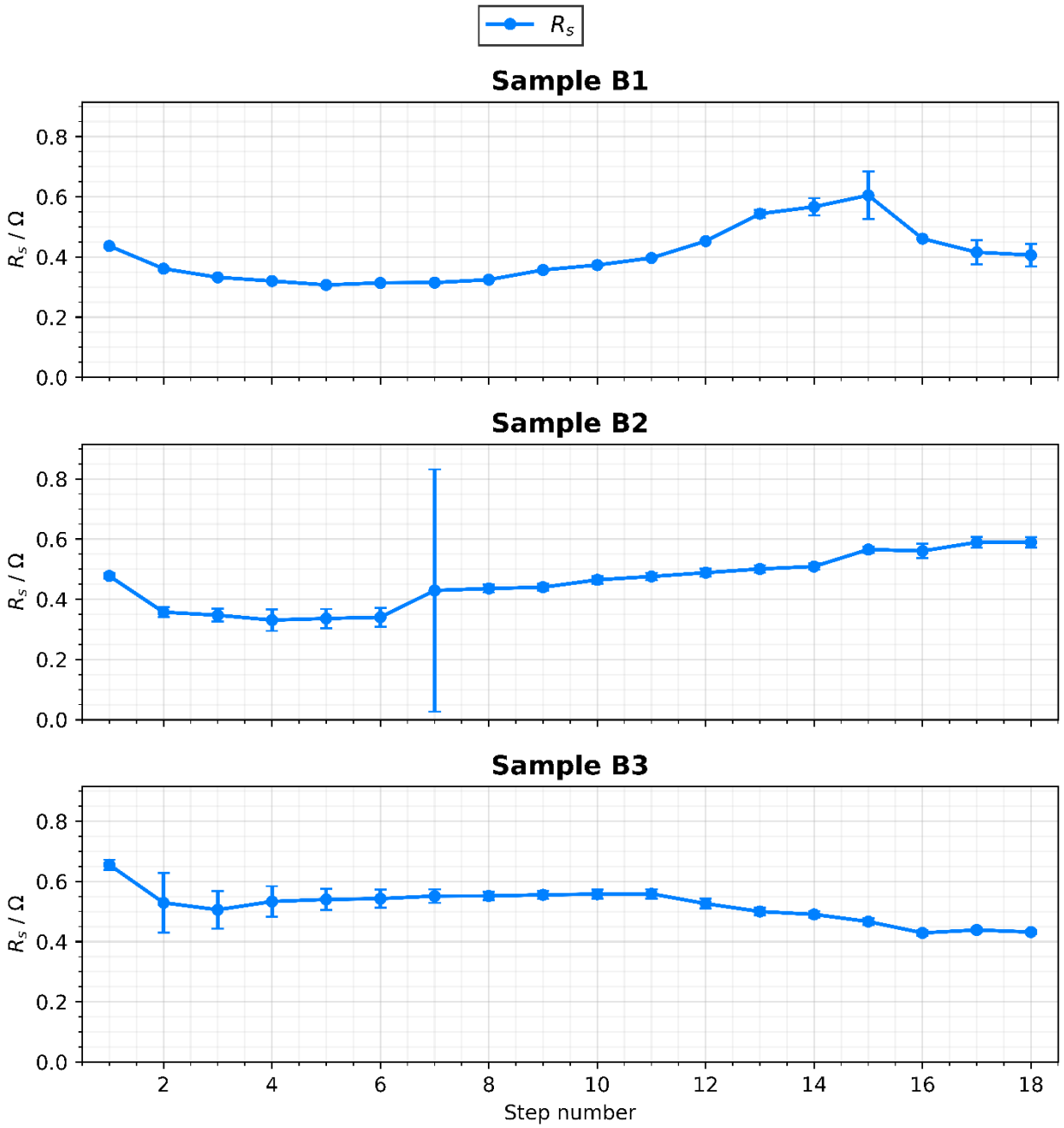


Fig. S5 - Evolution of the series resistance R_s extracted from equivalent-circuit fitting during ageing for samples B1, B2 and B3. Error bars represent the 95% confidence intervals obtained from the fitting procedure. The relatively limited variation of R_s compared with the changes observed for the polarization resistance indicates that the dominant ageing effects are associated with modifications of the electrode electrochemical response rather than with major changes in electrolyte conductivity or contact resistance.

Sample	R_s start	R_s end	R_{pol} start	R_{pol} end	ΔR_s (%)	ΔR_{pol} (%)
B1	0.437	0.406	0.582	4.25	−6.9	630.7
B2	0.478	0.589	1.11	1.29	23.4	16.1
B3	0.656	0.432	1.08	2.89	−34.1	168.8

Table S2 - Summary of the evolution of the series resistance (R_s) and polarization resistance (R_{pol}) during ageing for samples B1, B2 and B3. Initial and final values are reported together with the corresponding relative variation.

S6. Morphochemical modelling of chemical-state maps

The chemical-state maps can be mathematically modelled through parameter identification for the *morphochemical reaction-diffusion model*, also known as *DIB model*: a PDE model for electrochemical phase formation whose physico-chemical foundations are discussed in [2]. The restructuring of the electrocatalyst aggregate population resulting from ORR/OER cycling, giving rise to increased spatial heterogeneity, partial separation or redistribution of Mn and Ni, strong chemical reconstruction of the Ni-containing phase and potentially catalyst depletion near highly stressed regions [3-5], can be rigorously framed within the morphochemical theory underlying the DIB model. The shape changes of the electrocatalyst aggregates, coupled with potential-driven adsorption, can derive, among others, from the following mechanisms: MnO_2 restructuring and dissolution–redeposition under cathodic/anodic polarization, NiO transformation under OER conditions towards $Ni(OH)_2$/NiOOH-like phases, changes in oxide hydration and hydroxylation associated with the oxidation state and loss or redistribution of oxide particles due to carbon-support corrosion. In [6], we have shown that the DIB model yields a variety of spatio-temporal patterns depending on the model parameters. These patterns can be distinguished into two key classes: structured steady Turing patterns and unstructured dynamic Turing–Hopf patterns [7]. The spectral STXM and ptychography maps considered in this study can, in principle, be described by solutions of the DIB model obtained for suitable parameters belonging to the Turing–Hopf region, particularly in the neighbourhood of a codimension-two Turing–Hopf bifurcation point in the (C, B) parameter subspace [6]. Parameters C and B account for rate-determining potential-dependent adsorption and inhibition by adsorbates of electrochemically driven Mn(IV) redeposition from solubilized Mn(II) during OER and Ostwald ripening of Ni nanoparticles during ORR, respectively; extensive details are provided in [2, 8]. The extension to electrocatalysis requires a complex integration domain, since the electroactivity in the GDE active layer is confined to the electrocatalyst aggregates. This required dedicated numerical developments, detailed below. In this work, as a feasibility test and without loss of method generality, we have fitted two representative Mn chemical-state maps obtained by spectral STXM, corresponding to the Mn(II)/Mn(IV) and Mn(III)/Mn(IV) maps reported in Figure 6b of the main text. A systematic analysis of all STXM and ptychography maps would require a workload far beyond the scope of the present paper, which is centered on the development of spectral ptychography for electrocatalysis applications, and will be the subject of a forthcoming dedicated study. The mathematical fitting has been performed as follows.

Let $\theta_{exp}(x,y)$ be any experimental map. We normalize this map in [0,1] as follows:

$$\hat{\theta}(x,y) = \frac{\theta_{exp}(x,y) - \min\limits_{(x,y)} \theta_{exp}(x,y)}{\max\limits_{(x,y)} \theta_{exp}(x,y) - \min\limits_{(x,y)} \theta_{exp}(x,y)} \,. \qquad Eq.S1$$

The aforementioned DIB model is the following PDE system for the morphology $\eta(x,y,t)$ and the chemistry $\theta(x,y,t)$, with (x,y) denoting the space variables and t denoting the time variable (for formal details, see [2]):

$$\begin{cases} \dfrac{\partial \eta}{\partial t} = \Delta\eta + f(\eta,\theta); \\ \dfrac{\partial \theta}{\partial t} = d\Delta\theta + g(\eta,\theta), \end{cases} \qquad Eq.S2$$

where Δ denotes the spatial Laplace operator and the kinetics $f(\eta,\theta)$ and $g(\eta,\theta)$ are defined by:

$$\begin{aligned} f(\eta,\vartheta) &= A_1(1-\vartheta)\eta - A_2\eta^3 - B(\vartheta-\alpha); \\ g(\eta,\vartheta) &= C(1+k_2\eta)(1-\vartheta)[1-\gamma(1-\vartheta)] - D\theta(1-k_3\eta)(1+\gamma\cdot\theta). \end{aligned} \qquad Eq.S3$$

In (S3), A_1, A_2, k_2, k_3, α, γ are fixed positive parameters (see [7] for the exact values), while the positive parameters B, C (whose physical meaning is described above) are chosen in the Turing-Hopf region [6], and finally D depends on C according to the relation $D = \frac{C(1-\alpha)(1-\gamma+\gamma\alpha)}{\alpha(1+\gamma\alpha)}$. The DIB model (S2)-(S3) is completed by zero-flux boundary conditions and the following initial conditions:

$$\begin{aligned} \eta_0(x,y) &= \eta_{eq} + 10^{-4}\hat{\theta}(x,y); \\ \theta_0(x,y) &= \theta_{eq} + 10^{-4}\hat{\theta}(x,y), \end{aligned} \qquad Eq.S4$$

where $(\eta_{eq}, \theta_{eq}) = (0,0.5)$ is the spatially homogeneous equilibrium of the DIB model (S2)-(S3) and $\hat{\theta}(x,y)$ is the normalized experimental map defined in (S1). For a parameter pair (B,C) in the Turing-Hopf region [6] we solve the DIB model (S2)-(S3) with the initial conditions $(\eta_0(x,y), \theta_0(x,y))$ in (S4) and we call $\theta_n(x,y)$ the θ component of the numerical solution at the discrete time step $t_n, n = 1, \dots, N$. For all $= 1, \dots, N$ we normalize $\theta_n(x,y)$ in [0,1] as follows:

$$\tilde{\theta}_n(x,y) = \frac{\theta_n(x,y) - \min\limits_{(x,y)} \theta_n(x,y)}{\max\limits_{(x,y)} \theta_n(x,y) - \min\limits_{(x,y)} \theta_n(x,y)} \,. \qquad Eq.S5$$

We optimize in time (i.e. w.r.t. n) the L^2 error $\left\|\tilde{\theta}_n(x,y) - \hat{\theta}(x,y)\right\|_{L^2}$ and let $\tilde{\theta}^*(x,y)$ be the obtained optimal map at the corresponding optimal timestep t^*.

The above procedure is repeated for a selection of parameter pairs (B, C) in the Turing-Hopf region for both experimental maps considered in this Section. Some details of the numerical solution of the DIB model are as follows:

- We construct a triangular finite element mesh of the experimental maps in Fig. 6b in the main text. Specifically, each pixel of these maps is viewed as a square and split into two right triangles. See Fig. S6a.
- We refine the above mesh for higher spatial resolution. The resulting refined mesh is shown in Fig. S6b.
- We solve the DIB model (S2)-(S3) on the refined mesh using the Lumped Finite Element Method (LFEM) in space and IMEX Euler in time [9] implemented in MATLAB, ensuring both numerical stability and low computational cost.

We find the following fits:

- For Figure 6b (Mn(II)/Mn(IV)): $(B, C) = (110, 2.81)$, $t^* = 1.32$, L^2 error $= 19.47\%$. The experimental and the fitted maps are shown in Figs. S6c and S6d, respectively.
- For Figure 6b (Mn(III)/Mn(IV)): $(B, C) = (90, 2.79)$, $t^* = 1.10$, L^2 error $= 9.90\%$. The experimental and the fitted maps are shown in Figs. S6e and S6f, respectively.

To facilitate the comparison with the original maps in Fig 4b in the main text, the above numerical results for $\tilde{\theta}^*$ have been remapped to the original experimental range (see colorbars). From Figure S6, it can be noticed that the morphological features of both maps are fitted with good accuracy. A full discussion of the parameter estimates would require the systematic analysis of the whole corpus of maps, that will be published subsequently, but we can put forward that both the Mn(II)/Mn(IV) and the Mn(III)/Mn(IV) maps yield essentially the same C value, while the former map exhibits a larger B value. This can be straightforwardly explained with the fact that, on the one hand, the degradation of the ORR electrocatalyst renders the O_2-adsorption behavior of Mn(IV) the controlling factor, and, on the other hand, redeposition inhibition more strongly impacts the relative Mn(II)/Mn(IV) distribution with respect to the Mn(III)/Mn(IV) one, that is essentially controlled by oxidative desorption.

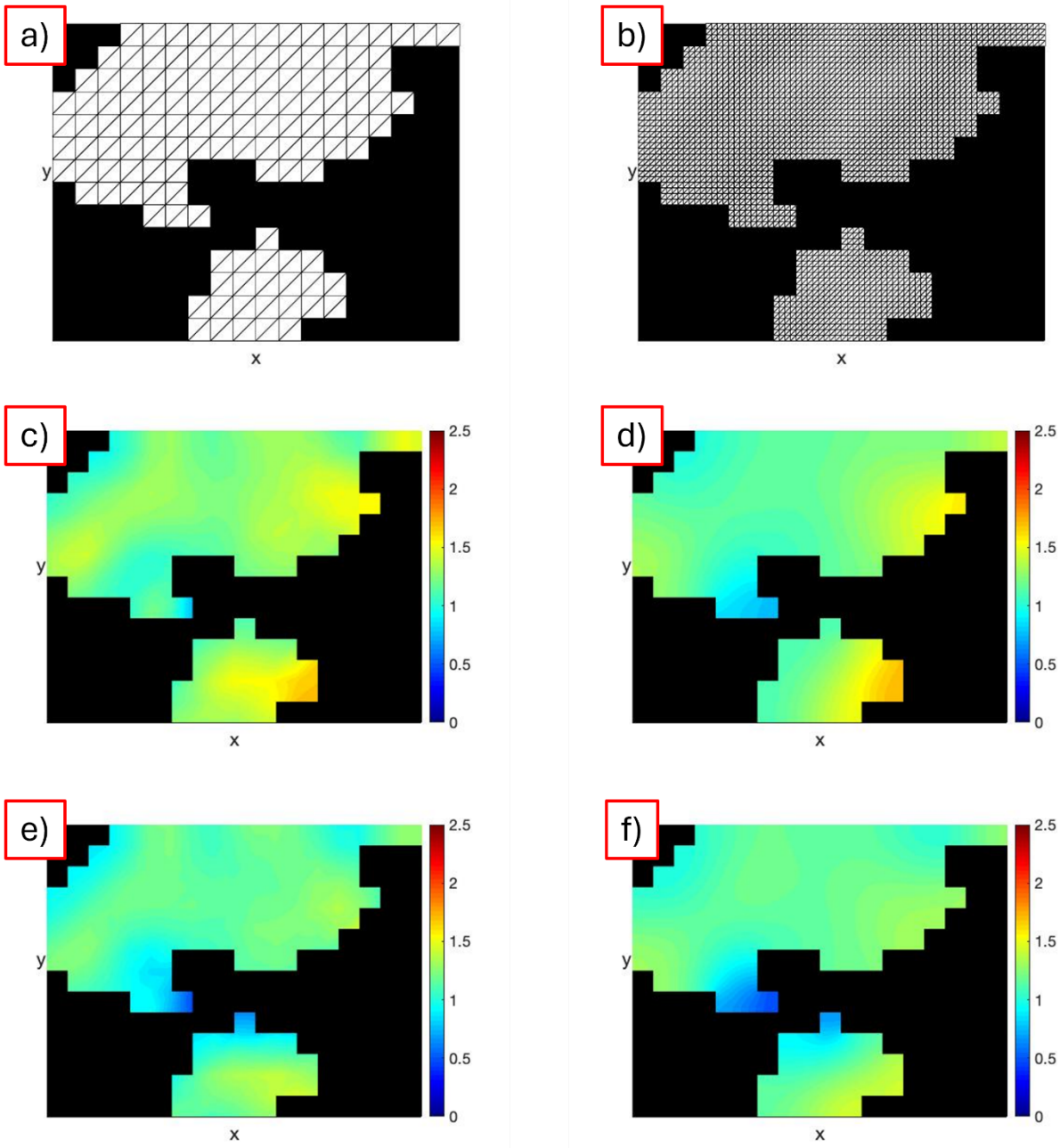


Figure S6. DIB model fitting of representative Mn chemical-state maps. (a) Coarse triangular finite-element mesh constructed from the experimental map and (b) corresponding refined mesh used for the numerical simulations. Experimental (left) and DIB-fitted (right) Mn(II)/Mn(IV) maps (c, d) and Mn(III)/Mn(IV) maps (e, f), respectively.

REFERENCES

[1] B. Watts. Calculation of the Kramers-Kronig transform of X-ray spectra by a piecewise Laurent polynomial method. *Optics Express* 22(19) (2014) 23628–23639. doi: 10.1364/OE.22.023628

[2] B. Bozzini, D. Lacitignola, I. Sgura. Spatio-temporal organization in alloy electrodeposition: a morphochemical mathematical model and its experimental validation. *Journal of Solid State Electrochemistry* 17(2) (2013) 467–479. doi: 10.1007/s10008-012-1945-7

[3] M. Kosin, S. Dondrup, J. Girschik, J. Burfeind, U. P Apfel, A. Grevé. Investigation of Highly Active Carbon-, Cobalt-, and Noble Metal-Free MnO2/NiO/Ni-Based Bifunctional Air Electrodes for Metal–Air Batteries with an Alkaline Electrolyte. *Global Challenges* 7(6) (2023) 2200223. doi: 10.1002/gch2.202200223

[4] H. M. Fernández, et al. Phase transitions in NiO during the oxygen evolution reaction assessed via electrochromic phenomena through operando UV–Vis spectroscopy. *Electrochimica Acta* 498 (2024) 144626. doi: 10.1016/j.electacta.2024.144626

[5] Y. Pei, W.Y. Wu, D.P. Wilkinson, E.L. Gyenge. High-Performance Reversible Oxygen Reduction/Evolution Gas Diffusion Electrodes with Multivalent Cation Doped Core-Shell Mn/Mn3O4 Catalysts. *ChemElectroChem* 11(3) (2024) e202300558. doi: 10.1002/celc.202300558

[6] D. Lacitignola, B. Bozzini, I. Sgura. Spatio-temporal organization in a morphochemical electrodeposition model: Hopf and Turing instabilities and their interplay. *European Journal of Applied Mathematics* 26(2) (2015) 143–173. doi: 10.1017/S0956792514000370

[7] I. Sgura, A.S. Lawless, B. Bozzini. Parameter estimation for a morphochemical reaction-diffusion model of electrochemical pattern formation. *Inverse Problems in Science and Engineering* 27(5) (2019) 618–647. doi: 10.1080/17415977.2018.1490278

[8] B. Bozzini et al. Depth-dependent scanning photoelectron microspectroscopy unravels the mechanism of dynamic pattern formation in alloy electrodeposition. *The Journal of Physical Chemistry C* 122(28) (2018) 15996–16007. doi: 10.1021/acs.jpcc.8b01267

[9] M. Frittelli, A. Madzvamuse, I. Sgura, C. Venkataraman. Preserving invariance properties of reaction–diffusion systems on stationary surfaces. *IMA Journal of Numerical Analysis* 39 (2019) 235–270. doi: 10.1093/imanum/drx058